Electrocatalysis (2017) 8:151–163
DOI 10.1007/s12678-016-0349-3

ORIGINAL RESEARCH

Understanding the Influence of the Biomass-Derived Alcohols on the Activity and Stability of Pt Nanoparticles Supported on Graphene Nanoribbons

Rodrigo Teles[1] · **Ana Arenillas**[2] · **Gabriel C. da Silva**[3] · **Pablo S. Fernández**[4] · **Eduardo S. F. Cardoso**[5] · **Gilberto Maia**[5] · **Cauê A. Martins**[1]

Published online: 7 January 2017

Abstract We produced Pt/GNRs by a one-step synthesis procedure and evaluated their electroactivity and stability towards glycerol electrooxidation reaction (GEOR) for the first time. We compared the electrocatalytic performance of GEOR with methanol and ethanol electrooxidation on Pt/GNRs at identical experimental conditions. The activities and stabilities for the electrooxidation of these biomass-derived alcohols on Pt/GNRs were compared to commercial Pt/C. The synthesis of the Pt/GNRs was confirmed by transmission electron microscopy, x-ray diffractometry, ultraviolet spectrophotometry, and Raman spectroscopy. We found that the activities of Pt/GNRs for these reactions are comparable to Pt/C, with improvement in terms of current density for methanol electrooxidation. Comparing potentiostatic measurements, we found that glycerol produces lower pseudo-stationary current densities than ethanol and methanol on both catalysts, with greatest values found for methanol electrooxidation on Pt/C. Otherwise, the GNRs remarkably enhance the stability of the catalyst for all the reactions, by increasing the stability of the current density during successive potential cycles, and by preventing the loss of electrochemically active surface area by avoiding carbon corrosion and Pt detachment. Moreover, we showed that the stability of the NPs depends on the biomass-derived alcohol used. The solution containing methanol reveals itself the most aggressive electrochemical environment to the catalyst, impacting in the decrease of surface area, while glycerol is less aggressive. Hence, the different products formed at the interface electrode/solution might lead to a different electrochemical environment, which plays an important role on the stability of the catalysts.

Keywords Pt-modified nanoribbons · Glycerol electrooxidation · Ethanol electrooxidation · Methanol electrooxidation · Electrochemical stability

Electronic supplementary material The online version of this article (doi:10.1007/s12678-016-0349-3) contains supplementary material, which is available to authorized users.

✉ Cauê A. Martins
caualvesmartins@gmail.com; cauemartins@ufgd.edu.br

[1] Faculty of Exact Sciences and Technology, Universidade Federal da Grande Dourados, 79804-970 Dourados, MS, Brazil

[2] Instituto Nacional del Carbón, CSIC, Apartado 73, 33080 Oviedo, Spain

[3] Instituto de Química de São Carlos/Universidade de São Paulo, IQSC-USP, C.P. 780, São Carlos, SP, Brazil

[4] Institute of Chemistry, State University of Campinas, 13083-970 Campinas, SP, Brazil

[5] Institute of Chemistry, Universidade Federal de Mato Grosso do Sul, C.P. 549, 79070-900 Campo Grande, MS, Brazil

Introduction

Biomass-derived alcohols such as methanol, ethanol, and glycerol have been investigated as potential fuels for direct alcohol fuel cells (DAFCs). These devices produce energy through a coupled electrochemical reaction, wherein the alcohol is electrooxidized at the anode while oxygen is electroreduced at the cathode [1]. The use of DAFCs is an environmentally friendly alternative to fossil fuels for the production of clean energy. However, several problems remain that pose a challenge for the commercialization of DAFCs: (1) the low activity and low tolerance to poisoning of Pt-based catalysts, (2) the high cost of precious metal nanocatalysts, (3) the substandard proton conductivity of the nanocatalysts, and (4) the low stability of the nanocatalysts. Among the challenges, finding an electrochemically stable catalyst seems to be the most critical. The electrochemical stability is directly

related to the electrochemical environment [2], changes in the nature of the metallic catalyst [3], and the nature of the carbon support [4] under operational conditions.

Carbon materials are used in fuel cells to anchor the metallic nanoparticles (NPs) and also work as electron collectors. The corrosion of carbon black, a commonly used commercial material, greatly contributes to the instability of both the cathodes and the anodes in fuel cells [5–9]. Alternative materials such as modified carbon black [10], mesoporous carbon [11, 12], carbon nanotubes [13, 14], carbon nanofibers [15], and graphenes [1] have been extensively studied as candidates to overcome the instability problem. Among these materials, metallic NPs immobilized on carbon nanotubes (CNTs), multiwalled carbon nanotubes (MWCNTs), and chemically converted graphene (CCG) have emerged as the most stable nanocomposites for fuel cell applications [1, 16–19].

Compared with CNTs and CCG, amorphous carbon black is thermochemically less stable and contains a high level of impurities [20], which results in poor electrocatalytic performance. In addition, while CNTs and CCG contain well-defined surface structures in a sp^2 network, carbon black has a high degree of superficial disorder [21]. Although CNTs exhibit high electrical conductivity, high durability, and low levels of impurities, the high aspect ratio and strong π–π interactions cause CNTs to form highly packed structures, hindering the uniform deposition of NPs onto the surface. The two-dimensional structure of CCG has similar characteristics to that of CNTs, while allowing the uniform deposition of NPs. The main disadvantage of CCG is the enveloping of NPs, which makes the NPs inactive. The enveloping of NPs represents decay in efficiency in terms of specific activity since part of the metallic content would not work properly, which might decrease the efficiency of the fuel cell.

Recently, we compared the electrochemical stabilities of carbon black-, CCG-, and MWCNT-modified Pd NPs in an alkaline medium by performing successive voltammetry cycles as a test protocol [17]. Both CCG and MWCNTs enhanced the stability of the nanocomposite compared with carbon black. Furthermore, Pd/CCG was found to be electrochemically more stable during the early cycles, while the Pd/MWCNTs were more stable over the long term. These results were rationalized as a competition between the availability of the support for metallic agglomeration and the corrosion of the support itself. In other words, although CCG initially seems to be more stable, its flat surface allows continuous agglomeration of the NPs over a long period of time; in contrast, the MWCNTs have a steric limitation for agglomeration and therefore do not continuously agglomerate NPs on their surfaces. Furthermore, in a DFT investigation, Staykov et al. showed that the binding interaction between the nanoparticles and the support is not significant on flat surfaces but significant on curved surfaces [22]. These authors reported that the chemisorption of NPs on CNTs prevented aggregation, whereas agglomeration of NPs on graphene under high temperatures caused a decrease in stability over time [22]. Considering the importance of both longitudinal curved surfaces and flat surfaces, a question emerges: why not combine the characteristics of both materials into one nanocomposite?

The Tour's group [23, 24] introduced a new method to produce graphene-based supports by a simple process for synthesizing graphene nanoribbons (GNRs). Nanoribbons combine the longitudinality of nanotubes and the flat surface of graphene. Such process can be divided in two steps. First, the MWCNTs are strongly oxidized, forming the so-called oxidized graphene nanoribbons (GONRs) [25]. In this step, the walls of the oxidized nanotubes are opened longitudinally, in a process called "unzipping" [23, 25]. Second, the GONRs are chemically reduced to produce GNRs. The proposed mechanism for the "unzipping" process is described elsewhere [23]. The longitudinal 2D surface (high length-to-width ratio) of the GNRs changed the nature of the support from a semiconductor to a semimetal [26].

The steric and electronic properties of GNRs lead to advantageous electrochemical features. Lima and Maia showed that a wide variety of easily synthesized large area GNRs show high activity toward the oxygen reduction reaction (ORR) [27]. In a pioneer study, Wang et al. used in situ chemical co-reduction to produce Pt/GNRs that showed excellent activity toward the methanol electrooxidation reaction (MEOR) [28]. However, no studies of the activity and stability of Pt-modified GNRs towards glycerol electrooxidation have been reported to date and, to the best of our knowledge, there is no work comparing the electrooxidation of methanol, ethanol, and glycerol. Moreover, the different experimental setups used in the distinct reports make the comparison of the alcohol electrooxidation very difficult. Here, we report a simple method for the one-step synthesis of Pt/GNRs for biomass-derived electrooxidation (methanol, ethanol, and glycerol) and an investigation of their electrochemical stabilities in the presence of the fuel. We present for the first time a thorough comparison of the electrooxidation properties of the alcohols on the Pt/GNRs.

Experimental

Synthesis of Graphene Oxide Nanoribbons (GONRs)

The GONRs were produced by a method adapted from Hummers and Offeman [29], as reported by Lima and Maia [27]. Briefly, 0.70 g MWCNTs (10 ± 1 nm OD, 4.5 ± 0.5 nm ID, 3–6 μm long, 6–8 tubes; Aldrich, used as received) were dispersed in 20 mL of concentrated H_2SO_4. Next, 0.37 g of $K_2S_2O_8$ and 0.37 g P_2O_5 were added to the solution, which was heated at 80 °C for 6 h under stirring. Then, the solution was cooled to room temperature and immersed in a water bath

at 0 °C. The product was filtered under vacuum through a 0.22-μm Nylon membrane while washing with water to achieve a neutral pH. The resulting pre-oxidized graphene nanoribbons were dried at room temperature.

Next, 0.70 g of the pre-oxidized graphene nanoribbons was re-oxidized [30] by adding 40 mL of concentrated H_2SO_4, 0.70 g of $NaNO_3$, and 2.10 g of $KMnO_4$ to the reaction flask at 0 °C. The mixture was held at 20 °C under stirring and then heated to 35 °C for 2 h. Next, we added 120 mL of water at 0 °C and 200 mL of water at 25 °C. Then 40 mL 30% H_2O_2 was added, and the mixture was stirred for at least 20 min. The solution was cooled to room temperature and transferred to a 3500-mL container of water at 0 °C. After 24 h, the precipitate was centrifuged and washed three times with (1) water, (2) aqueous HCl, and (3) water. The GONRs were obtained by filtration and washed with water on a Nylon membrane. Finally, the GONRs were dried in an oven at 30 °C, forming a powder.

Synthesis of Pt Nanoparticles Immobilized on Graphene Nanoribbons (Pt/GNRs)

The Pt/GNR NPs were produced by a one-pot synthesis from the GONRs, in a process based on previous reports [28]. First, 12 mg of the GONRs was dispersed in 12 mL water in an ultrasonic bath for 45 min. Then, 11.5 mg poly(acrylic acid) salt (PA, Mw = 2100) was added, and the dispersion was sonicated for at least 5 min. Any variation of this protocol should be performed while taking into account the ratio PA/Pt atoms = 3. Next, 2 mL of H_2PtCl_2 solution (10.6 mg mL^{-1}) was added to produce Pt/GNRs with a 40% metal loading, and the mixture was sonicated for 1 min.

The mixture was heated to 95 °C and purged with ultrapure N_2 for 10 min. Next, N_2 was removed from the solution and kept in the atmosphere of the reaction bath. Then 32 mL of $NaBH_4$ 0.5 mol L^{-1} was added, and the reaction bath was held at 95 °C in a N_2 atmosphere for 60 min. The reaction bath was allowed to spontaneously reach room temperature, and then the dispersion was washed with ultrapure water and centrifuged three times. Finally, the dispersion was dried for 24 h at 60 °C to produce the nanoparticle powder.

Electrode Preparation and Electrochemical Measurements

The dispersions of Pt/GNRs (ink) were prepared by adding 2 mg of powder to 1 mL water. To prepare the electrodes, 15 μL of the ink was deposited onto a 0.24-cm^2 Au electrode in order to produce a catalytic surface with 50 μg cm^{-2} loading (taking into account the mass of Pt on the Au electrode). To prepare the Pt/C (E-TEK, 40%) electrodes, we followed the same protocol, adding 10 μL of highly diluted Nafion® (1 mL 5% Nafion® in 20 mL 2-propanol) to the NPs immobilized on Au; this step was taken because the Pt/C NPs do not adhere as strongly to Au as do the Pt/GNRs. Prior to immobilizing the NPs on Au and start of the measurements, we carefully followed an electrochemical protocol to guarantee reproducibility and reliability, as detailed in Supplementary Information, Section I. Briefly, the Au disk was electrochemically cleaned and its electrochemical profile was registered. Figure S1 shows the characteristic profile of the bare Au. After the immobilization process, the Pt/C NPs were also electrochemically cleaned [31] and their profile recorded, as shown in Fig. S2.

The electrochemical experiments were carried out in a conventional three-electrode cell in an oxygen-free 0.5 mol L^{-1} H_2SO_4 solution using a potentiostat system (Potentiostat/Galvanostat μAutolab with current integration). A Pt plate with high surface area was used as counter electrode. The modified Au disk was used in a meniscus configuration as the working electrode. All potentials were measured against a reversible hydrogen electrode (RHE). The current densities (j) were calculated as the measured current divided by the electrochemically active surface area (ECSA), assuming 210 μC per square centimeter of Pt surface as the charge released by desorption of a hydrogen monolayer. All electrochemical experiments were performed in triplicate at 25 °C and all measurements were performed at least three times, and all parameters are given as averages with standard deviations presented as error bars to provide reliable information. To assess the electrocatalytic performance of the catalysts, we determined the onset potential and the potential peak from the first derivative of the voltammetry signal [32] and the current density peak directly from the voltammogram.

Evaluation of Biomass-Derived Electrooxidation and Stability Tests

We investigated methanol (MeOH), ethanol (EtOH), and glycerol (GlOH) electrooxidation on the Pt/GNRs and on 40% Pt/C E-TEK. The most important experimental detail is that the concentrations of the alcohols were selected to contain the same number of carbons (0.6 mol L^{-1} MeOH, 0.3 mol L^{-1} EtOH, and 0.2 mol L^{-1} GlOH). This experimental feature guarantees a reliable comparison among the output current densities, potentials (onset and peak), and electrochemical stabilities. It is well known that the chemical environment, pH, temperature, and concentration of reactants highly influence the pathways of the electrochemical reaction. In this sense, we followed exactly the same condition, at least much as possible, to compare the electrocatalytic parameters of the MeOH, EtOH, and GlOH electrooxidation on Pt/GNRs and Pt/C.

The electrochemical responses were measured in a solution containing 0.5 mol L^{-1} H_2SO_4 and X mol L^{-1} alcohol (where X is the alcohol concentration) at 0.05 V s^{-1} between 0.05 and

1.0 V. The starting potential was set to 0.12 V for all experiments to avoid the reduction of GlOH to propane [33] during the standby period. The representative feature of electrooxidation is shown as the fifth cycle, referred here as the stationary behavior. The onset potential determined from the first derivative [32] (not shown) was averaged from three independent measurements. Chronoamperometry experiments were performed by polarizing the electrodes at 0.12 V and stepping the potential to 0.6 V for 1800 s in the presence of the alcohol. The pseudo-stationary current densities are shown as an average of three independent measurements.

No standard protocol exists for evaluating the stability of potential anodes for direct alcohol fuel cells. A number of different methods have been reported in the literature. Chronoamperometry is often used to evaluate the stability of a catalyst toward the production of an electrochemical current over time [34]; however, such method does not mimic the start-up and shut-down processes found in fuel cells. To overcome this issue, one option is to measure the decay in electrochemically active surface area in the presence of the electrolyte during several cyclic voltammetry cycles over a wide range of potentials [9, 17, 35]. Although reliable, this approach is not ideal because it is usually performed in the absence of fuel. Here, we will show that the current density of the anodic process must be measured [36] concomitantly with the surface area. Here, we measured the current densities during the alcohol electrooxidation at a given potential over 1000 cyclic voltammetry cycles between 0.3 and 1.0 V at 0.3 V s^{-1} (in alcohol + electrolyte). Moreover, we recorded a profile (between 0.05 and 1.2 V at 0.05 V s^{-1}) in the presence of only electrolyte before and after the stability tests, which allowed us to determine the surface changes caused by the application of electric potential in the presence of fuel.

Physical Characterization of Pt/GNRs

The chemical composition of the Pt/GNRs was determined using a scanning electron microscope (Phenom ProX) connected to an energy dispersive x-ray spectrometer (EDS). The porosities of the GONRs and the Pt/GNR NPs were measured by physical adsorption of N_2 at −196 °C with an adsorption analyzer (Micromeritics Tristar 3020) after degassing the samples at 120 °C and 0.1 mbar for 8 h using a degasser (Micromeritics VacPrep 061). The following parameters were obtained: surface area (S_{BET}) and micropore volume (V_{micro}), calculated with the Brunauer–Emmett–Teller (BET) [37] and Dubinin–Radushkevich (DR) equations [38], respectively; total pore volume (V_p), estimated from the amount of N_2 adsorbed at $p/p° = 0.99$; and pore size distribution (PSD), determined by a density functional theory (DFT) calculation.

The crystallographic structures of the GONRs and Pt/GNRs were investigated by x-ray diffraction (XRD), using a Bruker D8 powder diffractometer equipped with a monochromatic Cu-Kα x-ray source; scans were performed with a step size of 0.02° in the 5–90° range and an interval of 2 s between steps. The disorder of the carbon supports was determined by Raman spectroscopy using a LabRAM HRUV 800 (JYV-Jobin Yvon) with a microscope (Olympus BXFM-ILHS) and an argon laser (CDPS532M, 532 nm at 24.3 mW). The analysis was performed between 800 and 3500 cm^{-1} with two 12-s accumulations.

The reduction of the GONRs to form GNRs was analyzed by ultraviolet spectroscopy. For the measurement, 50 μL of the 2 mg mL^{-1} dispersion was diluted to 5 mL, and the ultraviolet absorption was measured between 200 and 800 nm; the response is shown as an average of six measurements.

The morphologies and sizes of the nanoparticles and carbon supports were analyzed using a transmission electron microscope (TEM) (JEOL JEM2100) with a LaB_6 filament operating at 200 kV. Samples were prepared for TEM analysis by dispersion in 2-propanol and deposition onto a 400-mesh copper grid. The images were evaluated using the software Axio Vision SE64 Rel.4.8.

The wettability of the catalysts, which is related to the hydrophobic or hydrophilic interaction between the electrolyte + fuel solution and the carbon supports, was investigated by measuring the contact angle. We used a 4-μL droplet of the solution containing the electrolyte and fuel, holding constant the total number of carbons in solution for MeOH, EtOH, and GlOH to avoid a significant contribution from the viscosity of the alcohols. The droplet was placed on a thin film (made with 9 μL of the inks) and dried overnight on a glassy carbon plate (previously polished to a mirror finish). The detailed experimental procedure is described in Fig. S3.

Results and Discussion

Physical Characterization: Production of Pt/GNRs

The chemical composition of the Pt/GNRs determined from an average of eight measurements was 38 ± 3% metal loading on carbon (% weight of Pt). Hence, the synthesized and the commercial material have approximately the same amount of Pt on carbon, which diminishes the contribution of the metal loading on the comparison of activity and stability.

The production of the Pt NPs-modified GNRs from the GONRs via one-step synthesis was evaluated by Raman and ultraviolet spectroscopy, as shown in Fig. 1. As depicted in Fig. 1a, both the GONRs and the Pt/GNRs exhibit D and G bands at ~1332 and ~1595 cm^{-1}, respectively. The D band can be attributed to either disorder or sp^3 carbon hybridization, and the G band is attributed to energy level splitting associated with the E2g stretching mode of graphite [39]. Since a defect-free graphite structure should not have a D band, the structures of the GONRs and Pt/GNRs must exhibit some disorder. The increase in the degree of disorder was determined by

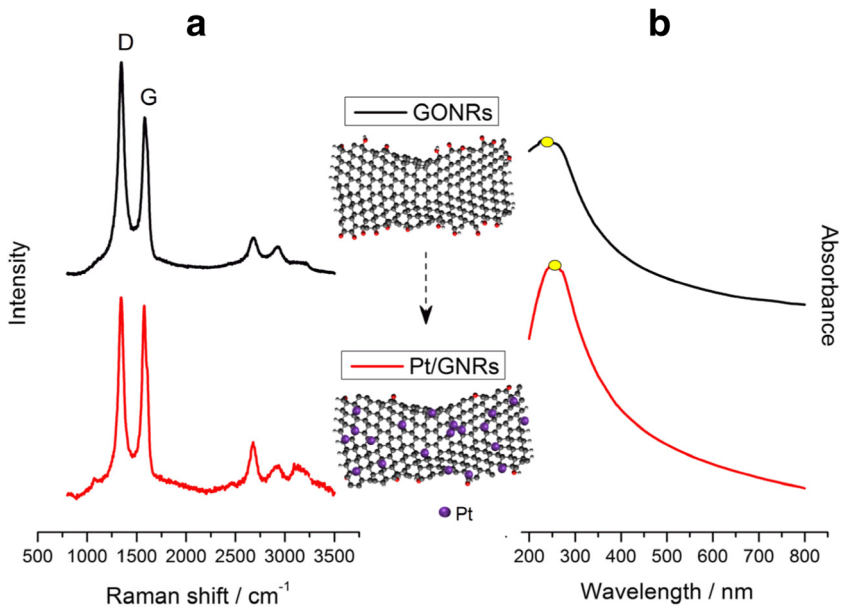

Fig. 1 **a** Raman spectra of GONRs and Pt/GNRs and **b** ultraviolet spectrum of an aqueous solution of GONR (*black*, λ_{max} 239 nm) and Pt/GNRs (*red*, λ_{max} 258 nm)

measuring the change in the ratio I_D/I_G [28, 40–42]. Figure 1a clearly shows that the I_D/I_G ratio decreases from 1.35 to 1.05, which indicates augmentation of the G network after the reduction of superficial groups containing oxygen. The second harmonic of the D band, referred to as the 2D band [43], appears as a shoulder at ~2680 cm^{-1} in both materials due to the graphite-like characteristics.

The ultraviolet absorption spectra show a bathochromic shift from 239 nm for the GONRs to 258 nm for the Pt/GNRs (Fig. 1b), indicating recovery of the electronic conjugation of the nanoribbons. The ultraviolet absorption spectrum is consistent with the literature [23] and with the results from Raman spectroscopy. The results of the structural characterization by XRD are shown in Fig. 2. The two diffraction peaks at 25.0° and 45.0° correspond to the (002) and (100) planes of the GONRs. The strong diffraction peaks at ~40.0°, 45.5°, 67.5°, 81.5°, and 86.0° for the Pt/GNR material are assigned to the (111), (200), (220), (311), and (222) facets of the face-centered structure of the Pt crystallites, respectively. The reduction of the GONRs to flat carbon surfaces containing metal nanoparticles hinders the C (100) diffraction peak and both decreases the intensity and broadens the width of the C (002) peak. Low-intensity peaks between 10.0° and 37.0° was previously reported for GONRs treated with $NaBH_4$ [28]

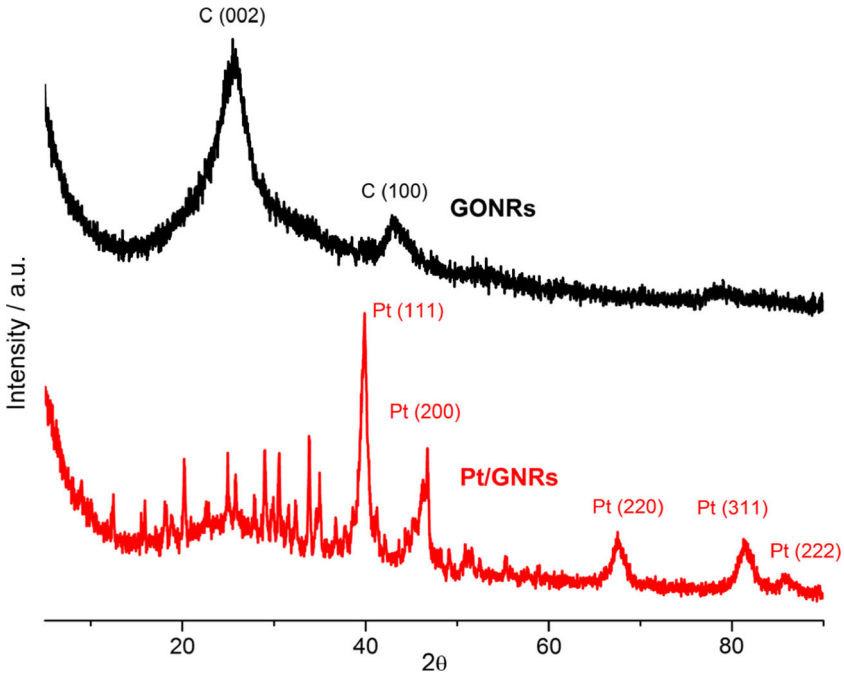

Fig. 2 XRD patterns of GONRs (*black*) and Pt/GNRs (*red*)

and for electrochemically produced Pt NPs shell decorating graphene (Pt NPs@G) from Pt NPs@GO [44]. The presence of Pt oxides [45, 46] and residual graphene oxides results in several low intensity peaks between 10.0° and 37.0°.

The N_2-adsorption isotherms of the catalysts are shown in Figs. S4 and S5. Both GONR and Pt/GNR materials can be classified as type IV, according to BDDT (Brunauer, Deming, Deming, and Teller) classification [47], with a hysteresis loop at high relative pressures indicating the presence of mesopores (see Fig. S4). Both isotherms have similar shapes at high relative pressures, indicating similar pore sizes, as shown by the pore diameters (d_{pore}) in Table 1. However, the materials adsorb different volumes of N_2, especially at low relative pressures. These observations are corroborated by the porosity parameters shown in Table 1.

Among all the parameters investigated here, the most affected by the reduction process and the deposition of the Pt NPs was the specific area (S_{BET}). The GONRs are composed of structures covered by functional groups that cause them to repel each other. After reduction, the loss of these groups produces flat structures that tend to stack on top of each other due to strong van der Waals interactions, diminishing the surface area available for N_2 adsorption. Another factor that contributes to the decrease in S_{BET} is the deposition of the Pt NPs. The NPs cover part of the ribbons, which blocks the penetration of N_2 into some regions of the porous structure.

The decrease in the mesopore volume (or increase in the size of the pores) is related to the decrease in the surface area of carbon in contact with the electrolytic solution, which is a crucial parameter in electrochemistry. Both materials are highly mesoporous, as shown by the micropore volume (V_{micro}) and mesopore volume (V_{meso}). The GONRs show considerable microporosity (pores < 2 nm) which leads to a large specific area (~205 $m^2\ g^{-1}$). The pore size distribution indicates that the porosities of the surfaces of both the GONRs and the Pt/GNRs are mostly in the mesoporous range (2–50 nm), and also indicates that the pore volume of the GONRs is high (Fig. S5). During reduction of the GONRs and deposition of the NPs, the same factors that diminish the specific area also diminish the porosity.

Microscopic Analysis: From MWCNTs to Pt/GNRs

The synthesis of the Pt/GNRs from the precursor MWCNTs was observed by TEM. The unzipping of the nanotubes is expected to increase the average diameter of the support as the nanoribbons begin to form. Figure 3a and d shows the TEM image and average diameter (9.4 ± 2.3 nm) for the MWCNTs. The value for the average diameter is in line with the value reported by the company providing the nanotubes (10 ± 1 nm). The average diameter of the support particles increased to 17.4 ± 3.9 nm after the oxidation process, when the GONRs were formed (Fig. 3b, e). The ~8.0 nm increase in the average diameter of the support proves the efficiency of the method for unzipping the nanotubes. The relatively large standard deviation is a consequence of the non-uniform nanoribbons since the outer and inner nanotubes of the MWCNTs have different diameters. Additionally, the partial unzipping of some nanotubes results in an increase in the heterogeneity and thereby increases the standard deviation.

Figure 3c shows the Pt NPs immobilized on the GNRs. The NPs had an average diameter of 5.0 ± 0.9 nm and mostly formed in small agglomerates. Hence, the average size and size distribution (Fig. 3f) were calculated using only the NPs with well-defined edges, which permitted to perform accurate measures. The deposition of the Pt NPs on the flat surfaces of the nanoribbons generates some defects on the surfaces, which work as nucleation centers for clustering (NCCs), as previously described for Pd deposition on chemically reduced graphenes [17]. As a result, the continuous deposition of Pt on the NCCs leads to the formation of small agglomerates. The reduced nanoribbons had an average diameter of 17.0 ± 2.5 nm, which indicates that the size of the support is not affected by the reduction process (Fig. S6). Figure S6 shows that the Pt NPs are more uniformly distributed on the carbon support than they are on the GNRs with few regions of agglomeration. Moreover, the average size of the Pt particles was 3.6 ± 0.7 nm, with sizes ranging from 2 to 7 nm.

Table 1 Porous characteristics of GONRs and Pt/GNRs

Sample	S_{BET} ($m^2\ g^{-1}$)	V_{micro} ($cm^3\ g^{-1}$)	V_p ($cm^3\ g^{-1}$)	V_{meso} ($cm^3\ g^{-1}$)	d_{pore} (nm)
Pt/GNRs	26.00	0.01	0.11	0.10	27.00
GONRs	205.00	0.07	0.41	0.34	25.00

Contact Angle (Wettability) Measurements

The wettability of the carbon material is determined by the nature (chemical composition) and structure (roughness) of the material [48]. Hence, the wettability is intrinsically related to the electroactivity of a catalyst since the reaction depends on the fuel and electrolyte having access to the active sites.

In general, a surface is defined as hydrophobic if the contact angle is >90° or hydrophilic if the contact angle is <90°. In this study, we minimized the contribution of the viscosity to the contact angle measurements by maintaining a constant number of carbons in the solution for all fuels. The average contact angles of the Pt/C and Pt/GNR catalysts for MeOH, EtOH, and GlOH in H_2SO_4 solution are given in Fig. 4.

Both the Pt/C and Pt/GNR catalysts are hydrophilic in all the alcohol solutions, as shown by the <90° angles. As expected, the hydrophilicity in MeOH was higher than that in EtOH due to the smaller organic chain of methanol and as a consequence of the non-oxidized carbon in ethanol ($-CH_3$). Comparing GlOH with EtOH, the contact angles reveal that

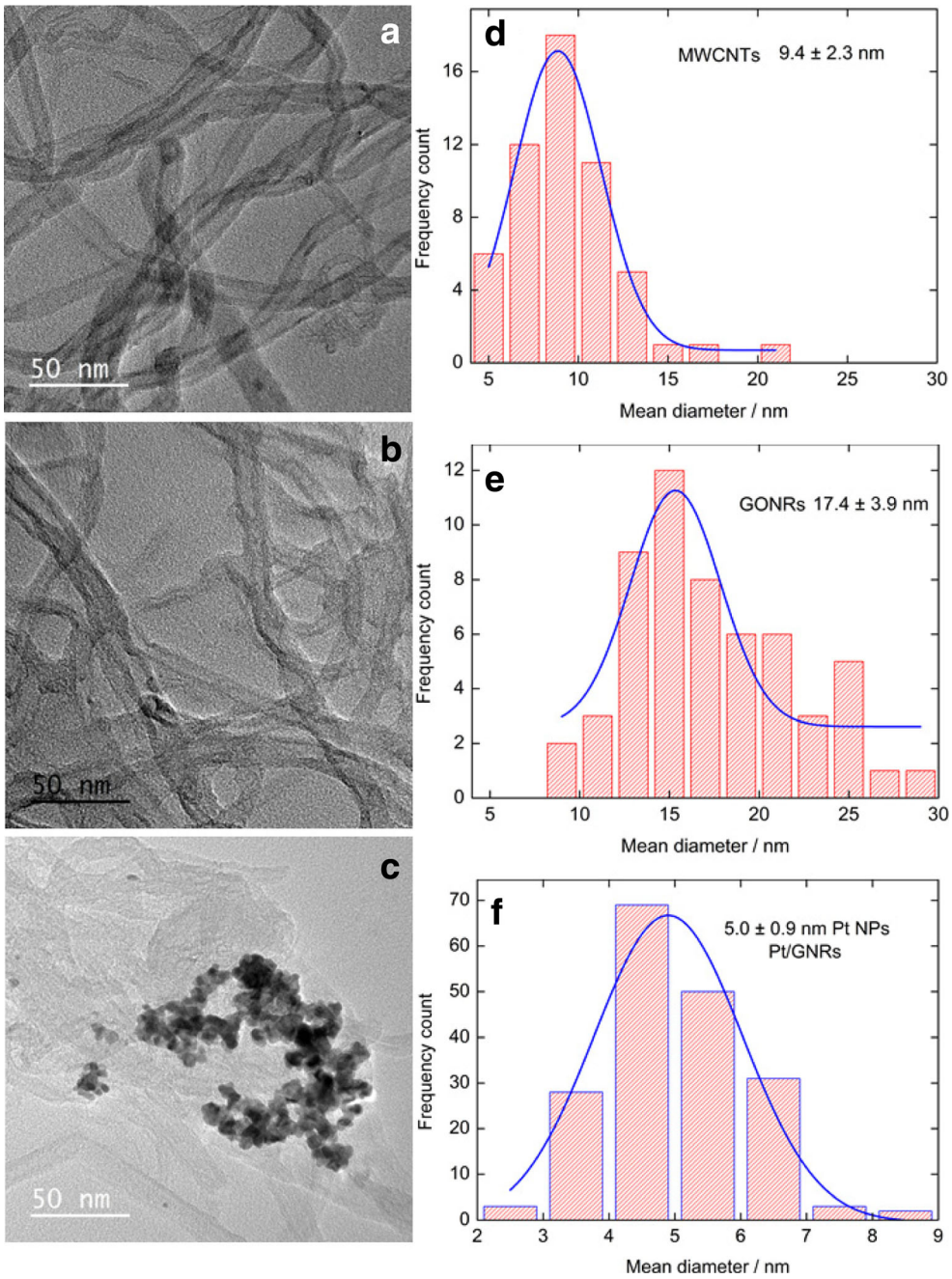

Fig. 3 TEM investigation of the synthesis of Pt/GNRs NPs. Micrographs and mean size diameter distribution of MWCNTs (**a** and **d**, respectively). Micrographs and mean diameter distribution of GONRs (**b** and **e**, respectively). Micrograph of Pt/GNRs (**c**) and mean size distribution of Pt immobilized on GNRs (**f**)

the three hydrated carbons in GlOH ($HOCH_2$–HCOH–H_2COH) facilitate the interaction with the catalysts, increasing their hydrophilicity. Pt/C surface in GlOH is slightly less hydrophilic than that in MeOH and more hydrophilic than Pt/GNR surface in GlOH. This observation suggests that GlOH (in H_2SO_4 solution) interacts well with GNRs compared with MeOH and EtOH. Interestingly, the Pt/GNRs had a higher contact angle than that of Pt/C for all fuels. The low hydrophilicity of the GNRs is a consequence of the extended Csp^2 network containing only a small amount of oxides on the surface, as well as the low surface area (26 $m^2\ g^{-1}$) compared to that of the commercial Pt/C material, which is ~150 $m^2\ g^{-1}$.

Now that the physical-chemical characterization of Pt/GNRs was presented, we dedicate the next sections to thoroughly investigate the activity and stability of Pt/GNRs compared to Pt/C for the alcohol electrooxidation.

Comparing the Activities of Biomass-Derived Electrooxidation on Pt/GNRs

As can be seen in the stable methanol oxidation electrochemical profile in Fig. 5a, the Pt/GNRs produced more current density than the Pt/C catalyst at potentials higher than 0.73 V during the forward scan and over the entire range of

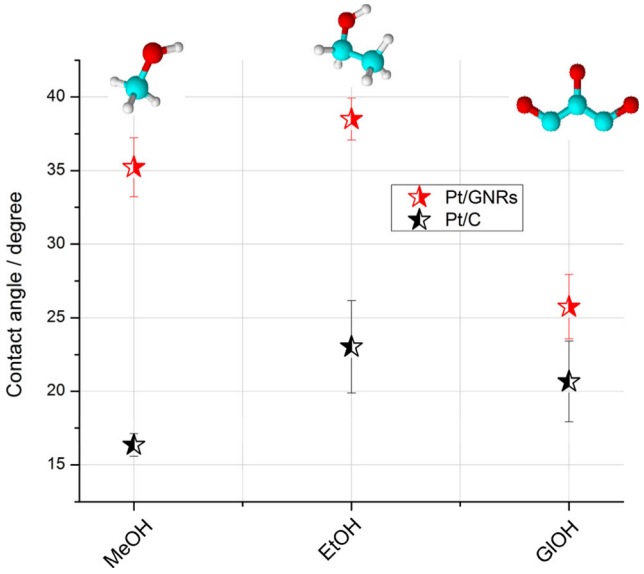

Fig. 4 Average contact angle of 0.6 mol L^{-1} methanol (MeOH), 0.3 mol L^{-1} ethanol (EtOH), and 0.2 mol L^{-1} glycerol (GlOH) in 0.5 mol L^{-1} H_2SO_4 on Pt/C and Pt/GNRs

potentials during the reverse scan. The peak current of the Pt/GNRs was ~2.3 times higher than that of the Pt/C. Chronoamperometry measurements (not shown) during 1800 s of polarization at 0.6 V (with a starting potential of 0.12 V) in the presence of MeOH showed that the average pseudo-stationary current density of the Pt/C was 1.5 times higher than that of the Pt/GNRs (0.057 and 0.038 mA cm^{-2}, respectively). The potentiostatic experiments corroborate the potentiodynamic measurements that the Pt/GNRs are more active only in higher potentials since it was performed at 0.6 V. The average onset potential calculated from the first derivative of the voltammetry signal [32] (dj/dE, not shown) was 0.66 V for the Pt/GNRs and 0.60 V for the Pt/C.

The increase in the current density of MEOR on the Pt/GNRs in the potentiodynamic experiment is in line with previous works investigating MEOR on graphene-based surfaces [28, 34, 35, 44]. Looking at the hydrogen under potential deposition H_{UPD} region (blank profiles) in Fig. 7, we can conclude that the NPs are essentially polycrystalline, and the Pt surface arrangements are very similar for both the Pt/GNR and Pt/C materials. Therefore, the important differences in the potentiodynamic behavior after 0.73 V are not caused by a different surface orientation of the metallic catalyst. The contribution of the substantial length of the nanoribbons to the electronic nature of Pt is probably the reason for the increase in the current densities, which is evidenced at potentials higher than 0.7 V. This result is in line with previous investigations of flat supports [34, 35, 44], although the onset potential is slightly delayed.

The same experimental protocol used to investigate MEOR was used for the EEOR analysis, but the alcohol concentration was adjusted to maintain the same number of carbons in solution (Fig. 5b). Both onset and peak potential are almost the same. The peak potentials in the forward scans were virtually the same for both catalysts. During the reverse scan, the anodic current is larger for the Pt/GNRs.

Chronoamperometric measurements (at 0.6 V for 1800 s) showed average pseudo-stationary current densities of 0.043 and 0.033 mA cm^{-2} for the Pt/GNRs and the Pt/C, respectively. The slightly increased activity of the Pt/GNRs in the potentiostatic experiments is a consequence of the slight lower onset potential since the voltammograms did not show any remarkable improvement during the forward potential scan.

Cyclic voltammograms in GlOH show comparable features for both catalysts (Fig. 5c). The onset potentials were virtually equal, 0.66 and 0.65 V for the Pt/GNRs and the Pt/C, respectively. The average pseudo-stationary current densities were also approximately equal (0.018 and 0.017 mA cm^{-2} for the Pt/GNRs and the Pt/C, respectively, after 1800 s at 0.6 V). The most relevant difference is in the peak potential of GEOR during the forward scan, which for the Pt/GNR material was located at a potential 40 mV lower than that of the Pt/C.

Comparing the Stabilities of Biomass-Derived Electrooxidation on Pt/GNRs

The stabilities of the catalysts, determined by measuring the current peak during 1000 potential cycles, are shown in Fig. 6.

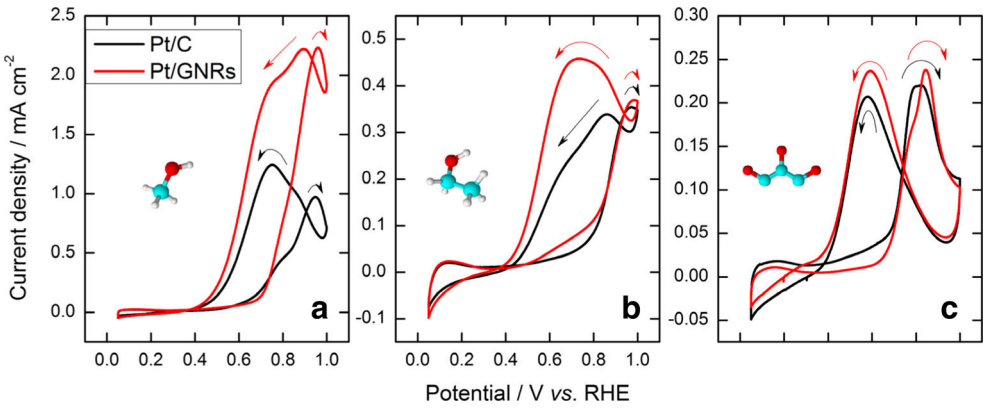

Fig. 5 Stable cyclic voltammograms of Pt/C and Pt/GNRs in 0.5 mol L^{-1} H_2SO_4 + **a** 0.6 mol L^{-1} methanol, **b** 0.3 mol L^{-1} ethanol, and **c** 0.2 mol L^{-1} glycerol between 0.05 and 1.0 V at 0.05 V s^{-1}

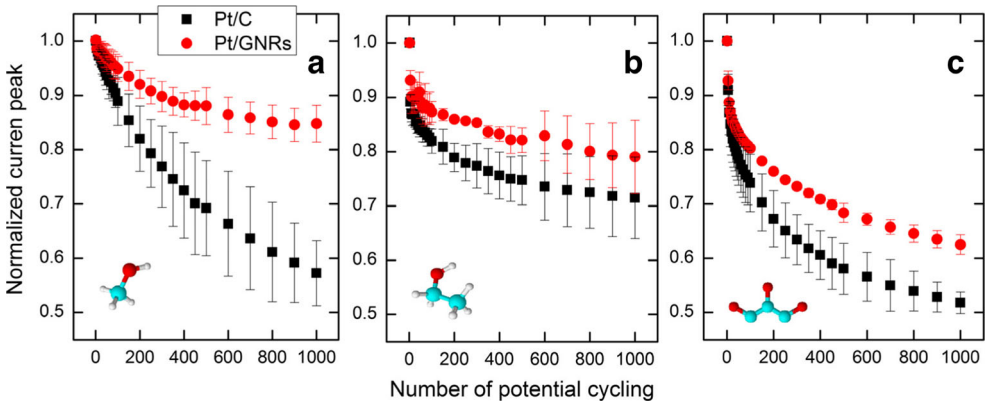

Fig. 6 Normalized current peak of the anodic current of the positive scan during 1000 potential cycles between 0.3 and 1.0 V at 0.3 V s^{-1}. Voltammograms obtained in 0.5 mol L^{-1} H_2SO_4 + **a** 0.6 mol L^{-1} methanol, **b** 0.3 mol L^{-1} ethanol, and **c** 0.2 mol L^{-1} glycerol

The Pt/GNRs are remarkably stable toward the MEOR reaction (Fig. 6a). After the degradation test protocol, the Pt/GNRs lose 15% of their initial activity, whereas the commercial material loses 43%. This result indicates a 28% improvement in the performance of the Pt/GNRs compared to Pt/C.

The Pt/GNRs displayed an increased electrochemical stability relative to that of the Pt/C for EEOR (Fig. 6b). The Pt/GNRs lose 21% of their initial activity, while the Pt/C loses 32%. However, the large standard deviation (error bars) in Fig. 6b suggests that similar performance might be achieved using Pt/C for EEOR, especially in the short term. Regarding the GEOR, we found that the Pt/GNRs lose 38% of their initial activity compared to 49% of loss for Pt/C, as shown in Fig. 6c. It is worth noting that the stability of the Pt/GNRs is remarkably reproducible (as shown by the small standard deviation).

The stability was also evaluated by monitoring the loss of ECSAs before (solid lines) and after (dashed lines) the successive cycles of biomass-derived electrooxidation, as shown in Fig. 7. The ECSAs obtained from the H_{UPD} region (Fig. 7a, b) change significantly after the stability tests in the presence of MeOH. ECSAs decrease ~20% for both Pt/GNR and Pt/C materials. Interestingly, the increase in the size of Pt (Δd(Pt)) was ~0.7 and ~0.6 nm for the Pt/C and Pt/GNRs, respectively (Fig. 7c, d). Histograms of the mean diameters calculated after the stability tests are shown in Fig. S7.

The increase in the size of the Pt NPs is not necessarily associated with the decrease in ECSA since the particles are agglomerated from the beginning. Another important factor that can contribute to the decrease in ECSA is the low stability of carbon Vulcan compared to nanoribbons. It is important to note that even though both electrodes lose about 20% of their ECSA after MEOR, the decrease in the activity of the Pt/C was larger than that of the Pt/GNRs (Fig. 6a). In other words, the current density was negatively affected to a greater degree

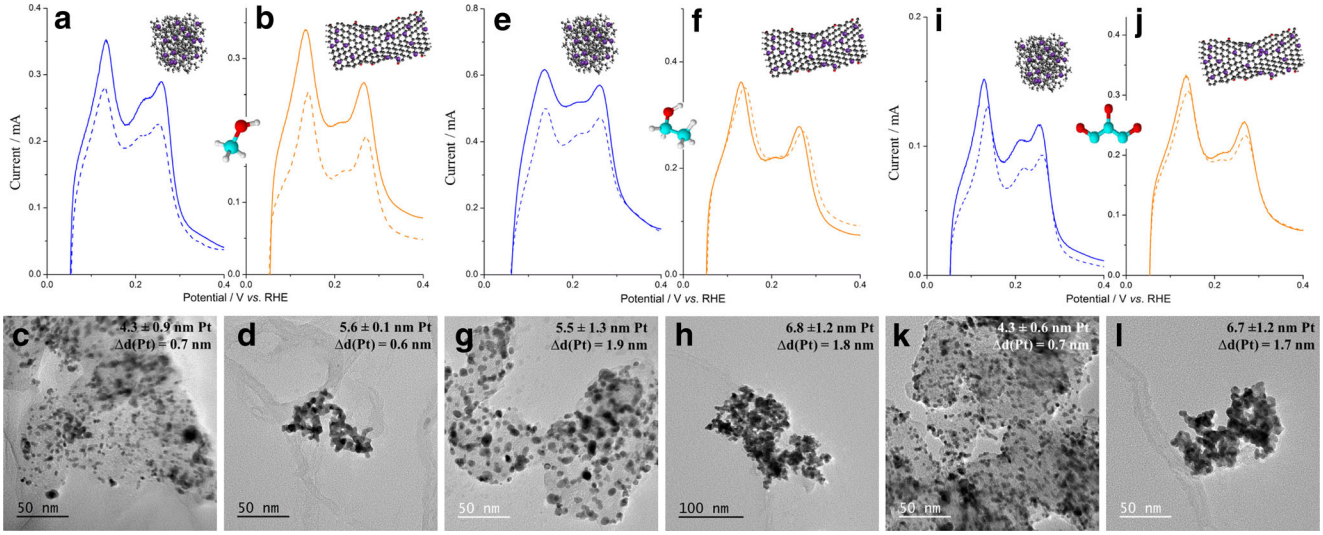

Fig. 7 Investigation of the electrochemical stability of Pt/C and Pt/GNRs (indicated by lustration) after 1000 potential cycles in 0.5 mol L^{-1} H_2SO_4 + **a**–**d** 0.6 mol L^{-1} methanol, **e**–**h** 0.3 mol L^{-1} ethanol, and **i**–**l** 0.2 mol L^{-1} glycerol. The hydrogen desorption regions of voltammetries recorded in 0.5 mol L^{-1} H_2SO_4 were obtained before (*solid lines*) and after (*dashed lines*) the degradation protocols. The micrographs show average sizes and NPs size increment after the tests

for the Pt/C than for the Pt/GNRs, which indicates that the degradation process not only affects the ECSA but also modifies the carbon surfaces as a consequence of carbon corrosion.

Figure 7e and f shows the ECSA of the catalysts before and after EEOR. It is clear that the decrease in ECSA is greater for the Pt/C than for the Pt/GNRs, as a consequence of the low average stability. As observed in the MEOR experiments, the Δd(Pt) values of the Pt/GNR and Pt/C materials in the EEOR experiments were similar (Fig. 7g, h). However, the values were larger than that for MEOR. This evidence suggests that the composition of the solution has an influence on the stability of the catalyst. Since the Δd(Pt) values are similar, the decrease in ECSA can be attributed to the detachment of the Pt NPs from the carbon surface, as was previously reported by identical-location TEM in the absence of fuel [2, 49].

The loss of area was also greater for the commercial material after GEOR, as shown in Fig. 7i and j. The micrographs reveal that the Δd(Pt) of the Pt/GNRs was 1.7 nm, while the Δd(Pt) of the Pt/C was 0.7 nm (Fig. 7k, l). The agglomeration effect in the Pt/GNRs causes the decrease in electrochemical stability. Here, we note that even though the particles were more agglomerated on the GNRs than on the carbon at the beginning of the experiment, the agglomeration was more intense on the GNRs, indicating that the presence of GlOH in the electrolyte has a different effect on the stability of Pt immobilized on different supports.

Considering the low Δd(Pt) of Pt/C, we infer that the detachment of Pt NPs, which was mainly caused by oxidation of the carbon support, added to the strong poisoning of the well-distributed Pt over the carbon black, were the main reasons for such a high loss of activity (49%) in the long-term experiments.

Here, we point out that we tentatively estimated the average width of the nanoribbons after the degradation test protocol for all reactions investigated, as shown in Fig. S7. Even though our estimation is quite rough as evidenced by the large standard deviation, we can infer that the widths of the nanoribbons were not significantly affected by the tests, although the chemical nature of the nanoribbons might be affected to some extent. Nevertheless, understanding the change in the electronic state and chemical composition of the GNRs is beyond the scope of this work. In the next section, we summarize the results of the Pt/GNRs for biomass-derived alcohol electrooxidation.

Evaluating the Activity and Stability of Pt/GNRs Toward Biomass-Derived Alcohols

Figure 8 shows the parameters related to the activity and electrochemical stability of the Pt/C and the Pt/GNRs toward MeOH, EtOH, and GlOH electrooxidation reactions under exactly the same experimental condition. Comparing the onset potentials for both catalysts in biomass-derived electrooxidation (Fig. 8a), we find that the EtOH electrooxidation reaction is clearly the least favorable. The non-oxidized $–CH_3$ makes C–C cleavage difficult. Moreover, the hydrophobicity caused by $–CH_3$ might obstruct the penetration into the active sites of the catalyst. Among all the alcohols, MeOH is the most likely to be oxidized. Comparing the Pt/C and the Pt/GNRs, we only found a slight difference in the presence of MeOH.

Another electrochemical parameter that helps to identify the activity of materials is the potential peak [32]. The potential peaks show similar values for MEOR and EEOR on Pt/GNRs and Pt/C NPs (Fig. 8b). GEOR shows lower potential peaks and the Pt/GNRs slightly shift the potential peak towards more negative values, although the onset potential is higher.

The current density peaks (j) determined from the first oxidation peak (Fig. 8c) indicate the activity under the influence of potential transients (dE/dt). The lowest values were found for GEOR, for which the Pt/GNRs and the Pt/C showed similar features. EEOR showed a higher j value than GEOR, also with similar values. Although more electrons might be extracted from GlOH than from EtOH, the sequential pathways of GEOR, involving several partially oxidized compounds, decrease the j value for GEOR on Pt surfaces, even considering that the same amount of carbon participates in the reaction [50].

MEOR exhibits the highest current densities, as a consequence of the diminished number of partially oxidized compounds. Interestingly, a very large increase in the j value was observed in the potentiodynamic experiment for MEOR on the Pt/GNRs compared to that for MEOR on the Pt/C, as a consequence of the improvements under elevated applied potential, since this peak appears at 0.95 V. This observation indicates that MEOR produces more output current than EEOR and GEOR in high potentials by using Pt/GNRs as catalyst.

The interpretation of the potentiostatic experiments using the pseudo-stationary j values, in Fig. 8d, reveals the weak performance of both catalysts for GEOR, which is consistent with the potentiodynamic experiments. EEOR displays higher j values than GEOR, and the Pt/GNRs showed higher j values than the Pt/C for EEOR. MEOR showed the highest j values, and the Pt/C was found to be the best catalyst in terms of the pseudo-stationary j value. Thus, with regard to MEOR, although the Pt/GNRs showed the highest j values during the potential sweep in high potentials, Pt/C showed better performance when the material experienced conditions similar to those of a fuel cell working under a low potential (onset).

Since the H_2SO_4 concentration was the same for all reactions, the decay of the ECSA was less dramatic when the catalysts were subjected to potential cycles in the presence of GlOH, as shown in Fig. 8e. MEOR represents the most unfavorable electrochemical environment, while EEOR presents intermediate values. The different products and intermediates produced in the different reactions change the interfacial pH accordingly [51], thereby modifying the

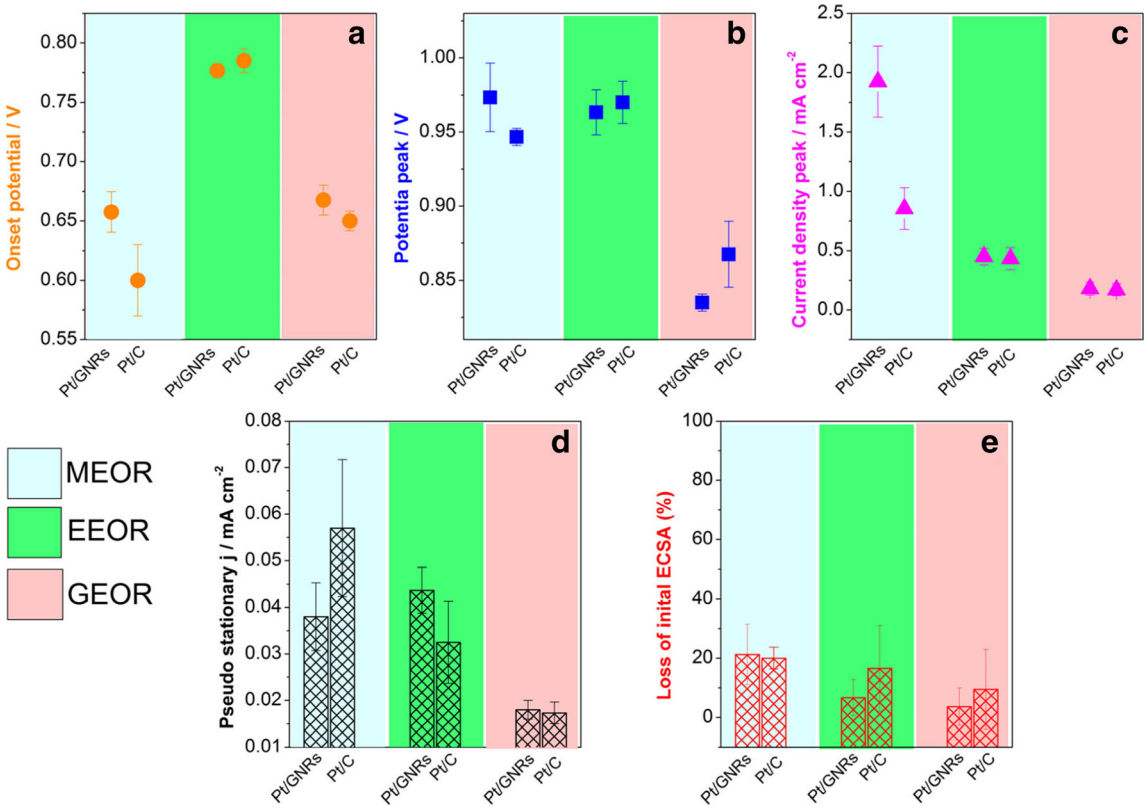

Fig. 8 Comparison of the electrochemical parameters regarding the methanol (MEOR, 0.6 mol L^{-1}), ethanol (EEOR, 0.3 mol L^{-1}), and glycerol (GEOR, 0.2 mol L^{-1}) electrooxidation reaction on Pt/C and Pt/GNRs nanoparticles. All measurements are shown as an average of three experiments with standard deviation (*error bars*). **a** Onset potential, **b** potential peak, and **c** current density peak obtained from the stable cyclic voltammogram of each alcohol in 0.5 mol L^{-1} H_2SO_4 between 0.05 and 1.0 V at 0.05 V s^{-1}. **d** Pseudo-stationary current density taken from current-time curves after 1800 s of polarization at 0.6 V (start potential of 0.2 V). **e** Average loss of electrochemically active surface area (ECSA) after 1000 potential cycles between 0.3 and 1.0 V at 0.3 V s^{-1}

electrochemical environment, which leads to different stabilities in terms of ECSA loss.

Theoretical calculations predict weak interaction between flat surfaces and metallic NPs [22] similar to those expected in the Pt/nanoribbons, so it is reasonable that the *d* band of Pt might be more available for reacting than the Pt immobilized on carbon black. This prediction, in addition to the high conductivity of the long double-bonded network, leads us to expect an improvement of activity in alcohols electrooxidized by Pt NP-modified nanoribbons. However, as reported by Brownson et al., graphenes might not be as electrochemically advantageous as they seem [52]; some characteristics might be desirable, but the overall performance might not be adequate for use in fuel cells.

The effectiveness of EtOH as a fuel is more strongly dependent than MeOH on the improvement in performance by multi-metallic catalysts. Assessing effectiveness of GlOH in fuel cells remains complicated, but the possibility of producing high-value compounds concomitantly with energy through the use of adequate catalysts [53, 54] increases the level of interest in such alcohol.

EtOH and GlOH seem not affected by the Pt-support interaction. Thus, the low activity of Pt/GNRs in EEOR and GEOR in acid media might be caused by the limited penetration of the fuel into the nanoribbon structures, caused by the sp^2 network as well as some wrapped ribbons attached to the small clusters of Pt on the nanoribbons.

In general, the stability of the Pt/GNRs in long-term experiments is improved compared to that of the Pt/C for all the biomass-derived alcohols. Nanoribbons assist Pt NPs in maintaining the activity through several cycles of use by preventing corrosion of the support and loss of surface area.

Summarizing, Pt/GNRs are advantageous materials to be used as anodes in direct alcohol fuel cells due to the long-term stability of the support, independent of the alcohol used. Therefore, the use of multi-metallic Pt-based catalysts immobilized on nanoribbons is a potential alternative for improving the electroactivity while maintaining the high electrochemical stability of the anode.

Conclusions

We successfully synthesized Pt-modified graphene nanoribbons (Pt/GNRs) from graphene oxide nanoribbons

(GONRs) by a $NaBH_4$ one-step method assisted by poly(-acrylic acid) salt. The Pt nanoparticles (NPs) were distributed in small clusters on the long flat surfaces. The average size of the individual NPs was approximately 5.0 ± 0.9 nm (with sizes ranging from 2 to 9 nm), and the NPs were dispersed over nanoribbons with an average width of 17.4 ± 3.9 nm.

Comparing the electroactivity of the Pt/GNRs with that of a commercial Pt/C in acid media, taking into account the same experimental conditions including the number of carbons in the solution, we found that the ethanol and glycerol electrooxidation reactions performed equivalently on both catalysts. Only the methanol electrooxidation reaction showed improved activity to some extent.

On the other hand, graphene nanoribbons substantially improve the ability of the catalyst to maintain an electrochemical response, and also improve the electrochemical stability, since GNRs prevent loss of electrochemically active surface area by preventing carbon corrosion and Pt detachment. Moreover, we found that the stability of the nanoparticles depends on the biomass-derived alcohol used, which is a variable rarely explored in the field. Among the reactions investigated, methanol electrooxidation in acid media appears to be the most aggressive environment for Pt nanoparticles supported either on carbon or on nanoribbons while glycerol media is less aggressive. Therefore, the different products formed at the interface electrode/solution might lead to a different electrochemical environment, which plays an important role on the stability of the catalysts.

Considering that the electroactivity toward biomass-derived electrooxidation can be tuned by alloying Pt with ad-atoms, GNRs are promising supports for multi-metallic nanoparticles used as anodes in direct alcohol fuel cells fed by MeOH, EtOH, or GlOH. The use of an ad-atom might improve the activity while GNRs improve the catalyst stability.

Acknowledgements The authors acknowledge financial assistance from CNPq (grant no. 454516/2014-2), FUNDECT (grant no. 026/2015), FAPESP (grant no. 2016/01365-0), CAPES, FINEP, and FAPESP. We thank Prof. Thiago Sequinel who helped in building the mini studio.

References

1. M. Liu, R. Zhang, W. Chen, Chem. Rev **114**, 5117 (2014)
2. A. Zadick, L. Dubau, N. Sergent, G. Berthomé, M. Chatenet, ACS Catal **5**, 4819 (2015)
3. L. Zhang, L.T. Roling, X. Wang, M. Vara, M. Chi, J. Liu, S.I. Choi, J. Park, J.A. Herron, Z. Xie, M. Mavrikakis, Y. Xia, Science **349**, 412 (2015)
4. P. Trogadas, T.F. Fuller, P. Strasser, Carbon **75**, 5 (2014)
5. S. Maass, F. Finsterwalder, G. Frank, R. Hartmann, C. Merten, J. Power Sources **176**, 444 (2008)
6. Y. Shao, G. Yin, Y. Gao, P. Shi, J. Electrochem. Soc. **153**, 1093 (2006)
7. Y.J. Wang, D.P. Wilkinson, J. Zhang, Chem. Rev **111**, 7625 (2011)
8. J. Ma, A. Habrioux, N. Alonso-Vante, ChemElectroChem **1**, 37 (2014)
9. J.C. Meier, C. Galeano, I. Katsounaros, J. Witte, H.J. Bongard, A.A. Topalov, C. Baldizzone, S. Mezzavilla, F. Schüth, K.J.J. Mayrhofer, Beilstein J Nanotechnol **5**, 44 (2014)
10. J.S. Noh, J.A. Schwarz, Carbon **28**, 675 (2002)
11. J.Y. Cheon, C. Ahn, D.J. You, C. Pak, S.H. Hur, J. Kim, S.H. Joo, J. Mater. Chem. A **1**, 1270 (2013)
12. J. Lee, S. Yoon, T. Hyeon, S.M. Oh, K.B. Kim, Chem. Commun. **21**, 2177 (1999)
13. A.C. Dillon, K.M. Jones, T.A. Bekkedahl, C.H. Kiang, D.S. Bethune, M.J. Heben, Nature **386**, 377 (1997)
14. P.S. Fernández, M.E. Martins, G.A. Camara, Electrochim. Acta **66**, 180 (2012)
15. A.L. Dicks, J. Power Sources **156**, 128 (2016)
16. F. Lima, G.V. Fortunato, G. Maia, RSC Adv. **3**, 9550 (2013)
17. C.A. Martins, P.S. Fernández, F. de Lima, H.E. Troiani, M.E. Martins, A. Arenillas, G. Maia, G.A. Camara, Nano Energy **9**, 142 (2014)
18. J. Zhang, S. Lu, Y. Xiang, P.K. Shen, J. Liu, S.P. Jiang, ChemSusChem **8**, 2956 (2015)
19. S. Stankovich, D.A. Dikin, R.D. Piner, K.A. Kohlhaas, A. Kleinhammes, Y. Jia, Y. Wu, S.B.T. Nguyen, R.S. Ruoff, Carbon **45**, 1558 (2007)
20. J. Wu, X.Z. Yuan, J.J. Martin, H. Wang, J. Zhang, J. Shen, S. Wu, W. Merida, J. Power Sources **184**, 104 (2008)
21. D.S. Su, S. Perathoner, G. Centi, Chem. Rev. **113**, 5782 (2013)
22. A. Staykov, Y. Ooishi, T. Ishihara, J. Phys. Chem. C **118**, 8907 (2014)
23. D.V. Kosynkin, A.L. Higginbotham, A. Sinitskii, J.R. Lomeda, A. Dimiev, B.K. Price, J.M. Tour, Nature **458**, 872 (2009)
24. Z. Zhang, Z. Sun, J. Yao, D.V. Kosynkin, J.M. Tour, J. Am. Chem. Soc. **131**, 13460 (2009)
25. A.L. Higginbotham, D.V. Kosynkin, A. Sinitskii, Z. Sun, J.M. Tour, ACS Nano **4**, 2059 (2010)
26. D.K. James, J.M. Tour, Acc. Chem. Res. **2013**(46), 2307 (2013)
27. F. de Lima, G. Maia, Nanoscale **7**, 6193 (2015)
28. C. Wang, H. Li, J. Zhao, Y. Zhu, W.Z. Yuan, Y. Zhang, Int. J. Hydrogen Energy **38**, 13230 (2013)
29. W.S. Hummers Jr., R.E. Offeman, J. Am. Chem. Soc. **80**, 1339 (1958)
30. N.I. Kovtyukhova, P.J. Ollivier, B.R. Martin, T.E. Mallouk, S.A. Chizhik, E.V. Buzaneva, A.D. Gorchinskiy, Chem Mater **11**, 771 (1999)
31. P.S. Fernández, D.S. Ferreira, C.A. Martins, H.E. Troiani, G.A. Camara, M.E. Martins, Electrochim. Acta **98**, 25 (2013)
32. A. Murthy, A. Manthiram, J. Phys. Chem. C **116**, 3827 (2012)
33. J. Schnaidt, M. Heinen, D. Denot, Z. Jusys, R.J. Behm, J. Electroanal. Chem. **661**, 250 (2011)
34. L.N. Zhou, X.T. Zhang, W.J. Shen, S.G. Sun, Y. Jun Li, RSC Adv **5**, 46017 (2015)
35. D.J. Chen, Q.L. Zhang, J.X. Feng, K.J. Ju, A.J. Wang, J. Wei, J.J. Feng, J. Power Sources **287**, 363 (2015)
36. K. Wu, Q. Zhang, D. Sun, X. Zhu, Y. Chen, T. Lu, Y. Tang, Int. J. Hydrogen Energy **40**, 6530 (2015)
37. S. Brunauer, P.H. Emmet, E. Teller, J. Am. Chem. Soc. **60**, 809 (1938)
38. M. Dubinin, Chem. Rev. **60**, 235 (1960)
39. H.-K. Jeong, Y.P. Lee, R.J.W.E. Lahaye, M.-H. Park, K.H.K. An, I.J. Kim, C.-W. Yang, C.Y. Park, R.S. Ruoff, Y.H. Lee, J. Am. Chem. Soc **130**, 1362 (2008)
40. B.F. Machado, A. Marchionni, R.R. Bacsa, M. Bellini, J. Beausoleil, W. Oberhauser, F. Vizza, P. Serp, J Energy Chem. **22**, 296 (2013)

41. J.I. Paredes, S. Villar-Rodil, P. Solís-Fernández, A. Martínez-Alonso, J.M. DTascón, Langmuir **25**, 5957 (2009)
42. I.K. Moon, J. Lee, R.S. Ruoff, H. Lee, Nature Communication **1**, 1 (2012)
43. A. Jorio, R. Saito, G. Dresselhaus, M.S. Dresselhaus, *Raman Spectroscopy in Graphene Related Systems* (Wiley-VCH Verlag GmbH & Co. KGaA, Weinheim, 2011)
44. Y.G. Zhou, J.J. Chen, F. bin Wang, Z.H. Sheng, X.H. Xia, Chem. Commun **46**, 5951 (2010)
45. E.E. Galloni, A.E. Roffo Jr., J Chem. Phys. **9**, 875 (1941)
46. O. Muller, R. Roy, J Less Common Met **16**, 129 (1986)
47. S. Brunauer, L.S. Deming, W.E. Deming, E. Teller, J. Am. Chem. Soc. **62**, 1723 (1940)
48. B.A. Kakade, V.K. Pillai, J. Phys. Chem. C **2008**(112), 3183 (2008)
49. F.R. Nikkuni, E.A. Ticianelli, L. Dubau, M. Chatenet, Electrocatal. **4**, 104 (2013)
50. C.A. Martins, P.S. Fernández, H.E. Troiani, M.E. Martins, G.A. Camara, J. Electroanal. Chem. **717–718**, 231 (2014)
51. R.S. Ferreira Jr., M.J. Giz, G.A. Camara, J. Electroanal. Chem. **697**, 15 (2013)
52. D.A.C. Brownson, L.J. Munro, D.K. Kampouris, C.E. Banks, RSC Adv. **2011**(1), 978 (2011)
53. Y. Kwon, Y. Birdja, I. Spanos, P. Rodriguez, M.T.M. Koper, ACS Catal. **2**, 759 (2012)
54. Y. Holade, K. Servant, T.W. Napporn, K.B. Kokoh, Electrochim. Acta **162**, 205 (2015)